PNAS
www.pnas.org

Supplementary Information for

Marine Ice Sheet Instability Amplifies and Skews Uncertainty in Projections of Future Sea Level Rise

Alexander A. Robel, Helene Seroussi, Gerard H. Roe

Alexander A. Robel
E-mail: robel@eas.gatech.edu

This PDF file includes:

Supplementary text
Figs. S1 to S5
Captions for Movies S1 to S4
References for SI reference citations

Other supplementary materials for this manuscript include the following:

Movies S1 to S4

Supporting Information Text

Stochastic Perturbation Theory

We take the stochastic perturbation approach outlined by Moon and Wettlaufer (1) and Fitzmaurice (2) for non-autonomous dynamical systems. We consider a system of the form

$$\frac{dL}{dt} = f(L,t) + \sigma_F \xi(t) \tag{1}$$

where $f(L,t)$ is the deterministic system dynamics, σ_F is the amplitude of stochastic forcing, and $\xi(t)$ is a Wiener process which is continuous in time, but can be approximated (for our purposes) as white noise when the system is numerically solved using the Euler-Maruyama method or similar. We assume the Martingale property wherein discrete increments of process $\xi(t)$ are uncorrelated in time.

The right hand side of equation 1 can be expanded in terms of a small perturbation, $\ell(t)$, about the solution to the deterministic version of the system, $L_d(t)$

$$\frac{d\ell}{dt} = \left[\omega\ell + \kappa\ell^2 + \ldots\right] + \sigma_F \xi(t) \tag{2}$$

where $\omega(t) = \frac{df}{dL}\bigg|_{L_d}$ and $\kappa(t) = \frac{1}{2}\frac{d^2 f}{dL^2}\bigg|_{L_d}$ are parameters that may be state- and time-dependent, and which define the leading-order behavior of the system. For equation 1 in the main text, these parameters are given by

$$\omega = \lambda b_x \left[P h_g^{-2} L + (\beta - 1)\gamma h_g^{\beta-2}\right] + P h_g^{-1} \tag{3}$$

$$\kappa = (\lambda b_x)^2 h_g^{-2} \left[P h_g^{-1} L + P(\lambda b_x)^{-1} - \frac{1}{2}(\beta-1)(\beta-2)\gamma h_g^{\beta-1}\right] \tag{4}$$

where $h_g = -\lambda b_g$ is the grounding line ice thickness, and $\lambda = \frac{\rho_w}{\rho_i}$.

We expand in terms of powers of the noise magnitude σ_F (where $\sigma_F << \ell$): $\ell = \ell_0 + \sigma_F \ell_1 + \frac{\sigma_F^2}{2}\ell_2$. The leading order terms describe initial perturbation from the deterministic solution of the system, and in general $\ell_0 = 0$ if the system begins on the deterministic trajectory (which we will take to be the case here, which greatly simplifies this analysis). The terms that are first-order in σ_F are

$$\frac{d\ell_1}{dt} = \omega(t)\ell_1 + \xi, \tag{5}$$

which can be written in the form of the Fokker-Planck equation

$$\frac{\partial \rho}{\partial t} = -\omega(t) + \frac{\partial}{\partial \ell_1}(\ell_1 \rho) + \frac{1}{2}\frac{\partial^2 \rho}{\partial \ell_1^2}, \tag{6}$$

where ρ is the probability density function of the first-order stochastic solution. We solve the Fokker-Planck equation in the typical fashion, by taking the Fourier transform in ℓ_1, solving the characteristic equation, and then re-inverting the Fourier transform. The result is a probability density function with second moment (variance)

$$\sigma_L(t)^2 = \frac{\sigma_F^2}{\Delta t} e^{2\omega(t)} \int_0^t e^{-2\omega(t)} ds. \tag{7}$$

This is the general nonlinear evolution equation for the spread of the stochastic PDF, which will provide the most accurate solution if ω is strongly time-dependent. However, we can solve for an approximate analytic form of the variance by assuming constant ω, which gives

$$\sigma_L(t)^2 = \frac{\sigma_F^2}{2\omega\Delta t}\left(e^{2\omega t} - 1\right), \tag{8}$$

which works fairly well soon after the onset of the instability and becomes a worse approximation over time (but captures the approximate rate of variance growth). Thus, we conclude that variance grows approximately exponentially with rate 2ω.

We note some features about the variance growth rate, ω (equation 3). The first term, which is typically the larger term (though not dominant) is proportional to the bed slope, b_x. Thus, the growth rate will generally increase with b_x, when it is positive (reverse-sloping bed). When b_x is sufficiently negative (forward-sloping bed), ω will also be negative, and the variance will remain bounded in time (though it won't necessarily go to zero). If we assume that the grounding line begins at a steady-state, then $PL = \gamma(-\lambda b_g)^\beta$, and we can simplify to $\omega = P h_g^{-1}\left(\beta\lambda b_x L h_g^{-1} + 1\right)$. It is important to note here that $\left(\beta\lambda b_x L h_g^{-1} + 1\right) = S_T$ is the same stability parameter (S_T) which is derived in Robel et al. (2018)(3), and which determines whether the slow time scale is stable or not (which is the only time scale in the model defined in equation 1 in the main text). Ice sheet geometry also matters in determining this growth rate, though this is, in some sense, fixed by the bed topography. Finally, β, the exponent for the grounding line flux also plays a role in determining the growth rate. Generally, the more nonlinear the grounding line flux is (e.g. for Coulomb plastic beds near the grounding line (4)), the more rapidly the ensemble variance will grow (see Figure S1). This should also be kept in mind when interpreting the results of the ISSM ensemble simulations in this study, which assume power-law sliding at the bed.

We can follow a similar procedure to solve the Fokker-Planck form of the equation for the terms that are second-order in σ_F: ℓ_2. This provides an analytical form of the third moment (skewness) of the probability density function (which was zero for the first-order terms):

$$Sk_L = \frac{\sigma_F^2}{\sigma_L^3 \Delta t} \left[-6\kappa S + 6\kappa \sigma_L^2 M + \sigma_F^2 \kappa^3 M^3 \right] \quad [9]$$

where

$$S(t) = \frac{\Delta t^2}{\sigma_F^4} e^{3\omega(t)} \int_0^t \sigma_L^4 e^{-3\omega(t)} ds \quad [10]$$

$$M(t) = \frac{\Delta t}{\sigma_F^2} e^{\omega(t)} \int_0^t \sigma_L^2 e^{-\omega(t)} ds. \quad [11]$$

This lengthy approximation is typically dominated by the second term in the minimal grounding line model, allowing us to drop the first and third terms to derive an expression for the skewness of the probability density function

$$Sk_L(t) = \frac{6\kappa M(t) \sigma_F^2}{\sigma_L \Delta t}. \quad [12]$$

Again, assuming that ω and κ are constant in time, we can solve the corresponding linear problem to derive a simplified approximate analytic form of the skewness

$$Sk_L(t) = 6\kappa\sigma_F \left[2\omega^3 \Delta t \left(e^{2\omega t} - 1 \right) \right]^{-\frac{1}{2}} \left(e^{\omega t} - 1 \right)^2 \quad [13]$$

The skewness is also dependent on ω through σ_L. However, critically, it is also proportional to κ. κ is proportional to b_x^2 meaning that skewness increases rapidly as the bed slope increases in magnitude, This is the case both for reverse- and forward-sloping beds, though as we showed above σ_L will remain sharply bounded for forward-sloping beds, and so will skewness. If we again make the assumption that the system begins at a steady-state ($PL = \gamma h_g^\beta$), then we can simplify the terms inside the brackets to: $PLh_g^{-1} \left[1 - \frac{1}{2} (\beta - 1)(\beta - 2) \right] + P (\lambda b_x)^{-1}$. This expression is dominated by the first term, in which the sign is set by $1 - \frac{1}{2} (\beta - 1)(\beta - 2)$. This is a quadratic expression which is positive for $0 < \beta < 3$ and negative for $\beta > 3$. In asymptotic analyses of the grounding line ice flux (4–6), this exact exponent is the target of considerable analysis. It is generally the case that $\beta > 3$, and often considerably so. Thus, we may conclude that the skewness of ensemble projections will generally be negative during the marine ice sheet instability, corresponding to ensemble projection distributions with a fat tail in the direction of more ice loss.

Figure S1 shows variation in ensemble statistics as a function of changing grounding line flux nonlinearity, β. This plot shows that the skewness is zero or positive (towards slower retreat) when $\beta \leq 3$ and that skewness becomes increasingly negative as β increases above 3.

Autocorrelated Forcing. Moon & Wettlaufer (1) invoke the Martingale property to simplify their approach to stochastic perturbation analysis, via an appeal to the Fokker-Planck equation (see **??**). The Martingale property assumes that the forcing is white nose, thus disallowing any autocorrelation in the forcing function. However, in reality, forcing from the ocean and atmopshere may be expected to have persistence at time scales longer than the forcing time step.

We can get a sense for the influence of autocorrelation in the time-dependent forcing function, by following the approach of Roe & Baker (7). For a first-order autoregressive discrete forcing process with autocorrelation coefficient $r = 1 - \Delta t/\tau_F$ (where τ_F is the decorrelation time scale), they derive a scaling for the expected spread of the prognostic variable (L in our case)

$$\sigma_L = \sigma_L^{r=0} \left[\frac{1 - r^2}{(1 - r)^2} \right]^{\frac{1}{2}} \quad [14]$$

where $\sigma_L^{r=0}$ is the ensemble spread for white noise forcing, derived in the section above. Thus, in terms of τ_F, the ensemble spread is

$$\sigma_L = \sigma_L^{r=0} \left[2 \frac{\tau}{\Delta t} - 1 \right]^{\frac{1}{2}}. \quad [15]$$

Strictly speaking, this added factor is derived for a stable auto-regressive model. However, it turns out to match numerically calculated values of σ_L for autocorrelated forcing (see Fig. 2 in the main text) sufficiently close to the initial steady-state condition, similarly to the linearized approximations for $\sigma_L^{r=0}$ calculated in section **??** which are good for some time after the onset of instability, and degrade after a sufficiently long period of unstable growth of the ensemble spread. However, it does not provide an analytical estimate for the skewness in the presence of autocorrelated forcing.

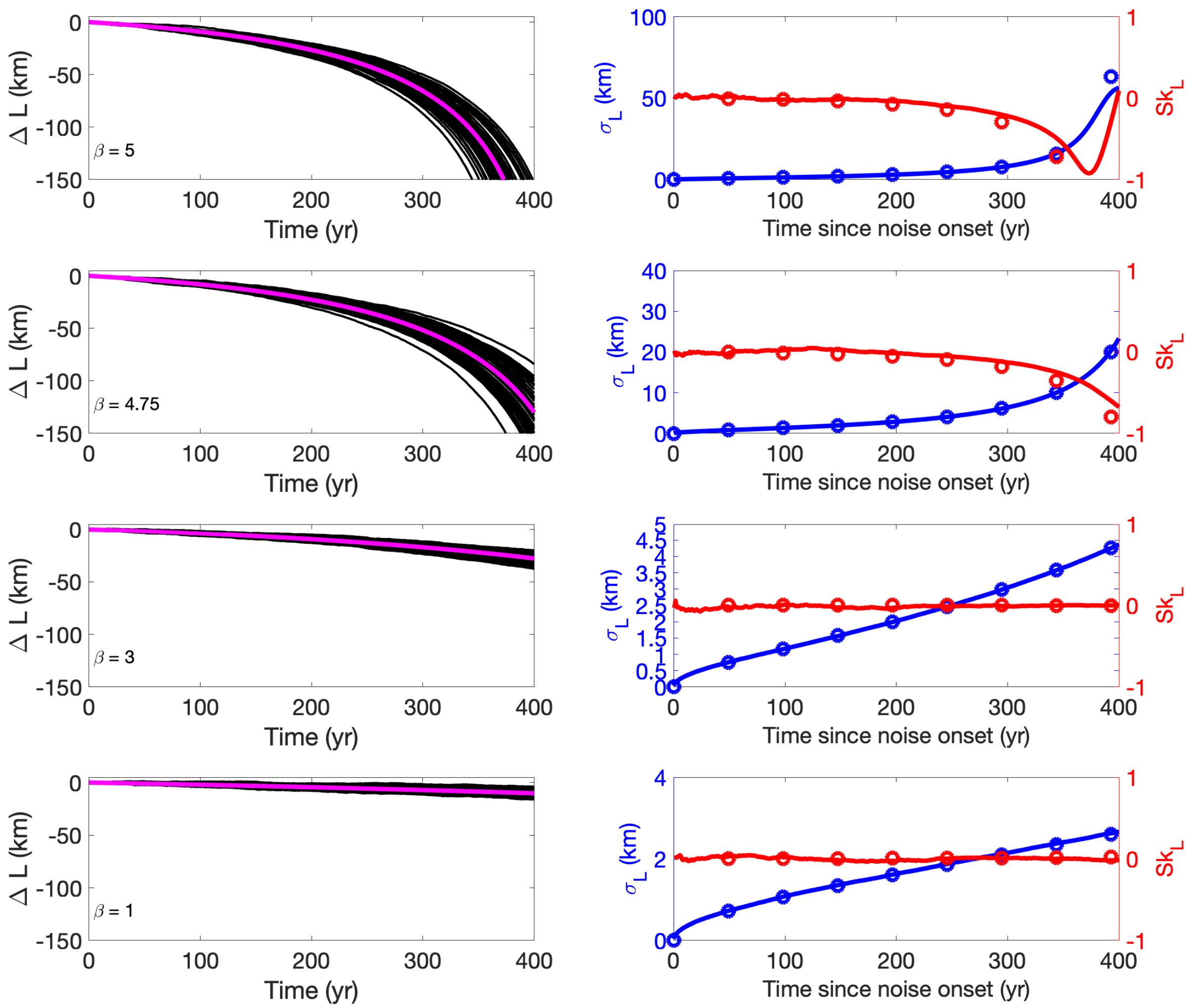

Fig. S1. Ensembles of grounding line retreat simulated with minimal prognostic model of grounding line migration (equation 1 in main text). In all simulations: $P = 0.35$ m/yr, $b_x = 3 \times 10^{-3}$. β and γ varied in each row to keep initial value of γh_g^{β} constant. (Left-side) Grounding line migration over different bed slopes. Black lines are 50 randomly-chosen ensemble members (out of 10000 used to calculate ensemble statistics). Magenta lines are simulations with $\eta = 0$. (Right-side) Ensemble statistics: standard deviation (blue), skewness (red, with more retreat being negative skew).

Ocean Model Simulation. The Massachusetts Institute of Technology general circulation model (MITgcm; (8)) was used to simulate the evolution of oceanic conditions in the Amundsen Sea over the 1992-2007 period. The simulation includes a thermodynamic sea ice model (9) and a representation of ocean induced melting and freezing parameterized as a diffusive flux of temperature and salinity (10, 11). The model relies on a global configuration that is part of the Estimating the Circulation and Climate of the Ocean, Phase II (ECCO2) project (12, 13). The model domain covers the Amundsen Sea Embayment, from Abbott to Getz ice shelves, and extends at least 100 km beyond the outer edge of the continental shelf, similar to the configuration in Seroussi et al. (14). The model grid is extracted from the 18 km Cube Sphere of Menemenlis et al. (12), downscaled to a 2 km horizontal grid spacing, and includes 46 uneven vertical levels, which constrains the time steps to 115 s. The initial and boundary conditions are interpolated from the ECCO2 integration (15), and the atmospheric forcing is constrained with the Japan Meteorological Agency and Central Research Institute of Electric Power Industry 25 year reanalysis (16) over the 1992-2007 period. A constant turbulent exchange and friction velocity coefficients is applied for the exchange of fresh water and heat at the ice shelf base (17), similar to Dinniman et al. (18), and Schodlok et al. (19, 20). Ice shelf cavities do not evolve during the simulation as the objective of this simulation is to assess the variability in oceanic conditions in ice shelf cavities, independently of changes happening over the ice sheet.

The dominant time scale of variability in the ocean model simulation is almost exactly one year, likely due to the dominance of the annual cycle in the forcing. Longer time scales are not present due to the absence of ocean-atmosphere coupling which tends to produce low-frequency modes of variability in fully coupled climate models in this region (21). We show the ensemble statistics for Thwaites Glacier with ocean forcing persistent at $\tau_F = 13$ months in supplemental Fig. 2. The interannual standard deviation of the maximum melt rate at depth is $\sigma_M = 1.4$ m/yr. However, it should be noted that calculations of standard deviation from time series depend on the time step under consideration. The inter-monthly standard deviation is 5 m/yr.

Ice Sheet System Model (ISSM) Configuration

ISSM is a finite element software package which is used to solve the two-dimensional shelfy-stream approximation for this study (22). It is publicly available for download from: https://issm.jpl.nasa.gov/. The model solves for ice velocity, surface and base elevation, and grounding line position at each time step. In our simulations, basal friction follows a linear viscous law and ice rigidity is a function of ice temperature, both are inverted on the basis of modern velocities (23) using data assimilation (24). Ice temperature, basal friction and basin boundaries (covering the Thwaites Glacier catchment) are held fixed throughout the simulation to reduce computational load and facilitate the large ensemble simulations. The horizontal resolution is 1 km over the entire catchment basin. Grounding line position is determined by a floatation criterion: ice is floating if its thickness is smaller than the floatation height and grounded otherwise. A minimum ice thickness is imposed to be 1 m everywhere, which contributes negligibly to buttressing. We use a subelement parameterization in order to accurately capture the position of the grounding line and integrate basal friction accurately over the grounded part of the domain(25). Sub-ice shelf basal melt follows a simple function of depth: $M(z) = M_{max} - M_{max}(z_{max} - z)$, where M_{max} is the maximum melt rate that occurs at a depth z_{max}. Melt is applied only to elements which are completely floating, which produces slower, but more rapidly-converged (to a benchmark solution) retreat rates (26). Two week time steps are used for all simulations, though perturbations in M_{max} are varied every month and renormalized to ensure that the standard deviation of monthly M_{max} is always 5 m/yr, regardless of the long-term persistence. Bedrock elevation and initial surface elevation for the ice streams and ice shelves are derived from a combination of Bedmap2 (27) and a mass conservation method (28). Surface mass balance and surface temperatures averaged over the 1979-2010 period from RACMO2 (29) are applied at the surface of the domain, and the geothermal flux used to compute the ice steady state temperature comes from Shapiro and Ritzwoller (30). Surface mass balance is held constant during all simulations.

Extended Results of ISSM Ensembles

In this section, we provide full diagnostic results for each ISSM ensemble of Thwaites Glacier simulation in the same format as Figure 3 in the main text. Each of these plots corresponds to one of the lines in Figure 4 of the main text, exploring how ensemble statistics change as a function of forcing persistence and uncertainty in the time-average forcing.

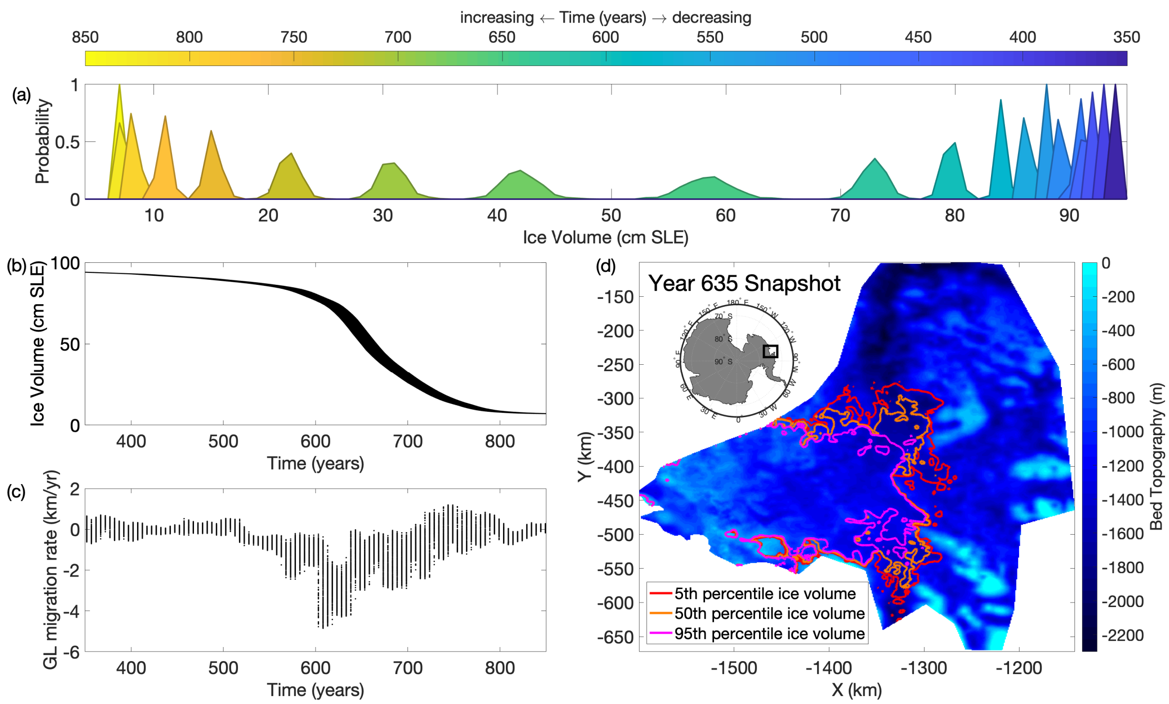

Fig. S2. Evolution of a 500-member ensemble of Ice Sheet System Model (ISSM) simulations of Thwaites glacier evolution over 500 years (where year zero in model time is the modern glacier state) in response to interannual variability ($\tau_F = 1.1$ yr) and constant average in maximum sub-ice shelf melt rate. (a) Evolution of ensemble probability distribution function (PDF) over time, plotted every 25 years, with probability on y-axis and Thwaites Glacier ice volume (in cm sea level equivalent; SLE) on x-axis. (b) Black lines are simulated ice volume contained in Thwaites Glacier catchment in cm SLE for all ensemble members. (c) Black dots are evolving grounding line migration rates for all ensemble members (based on the centroid of the 2D grounding line). (d) Snapshots (red, orange and pink lines) of grounding line positions at year 635 in model time, from 5th percentile, 50th percentile and 95th percentile ice volume ensemble members.

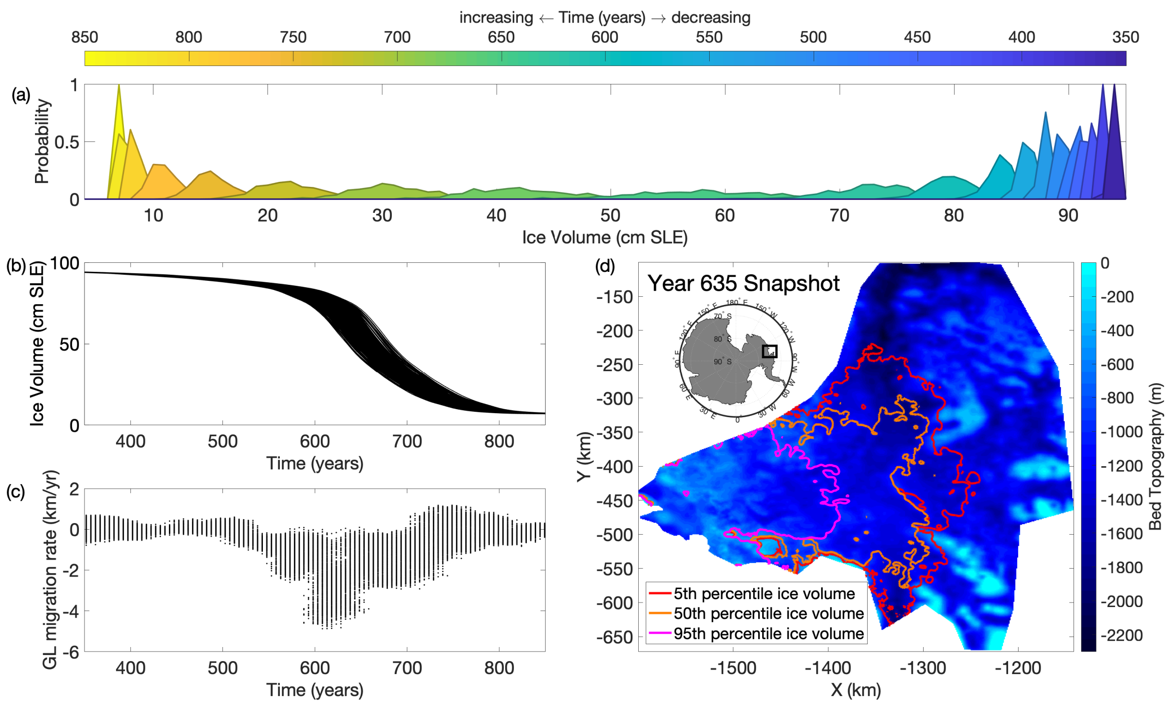

Fig. S3. Evolution of a 500-member ensemble of Ice Sheet System Model (ISSM) simulations of Thwaites glacier evolution over 500 years (where year zero in model time is the modern glacier state) in response to decadal variability ($\tau_F = 10$ yr) and constant average in maximum sub-ice shelf melt rate. (a) Evolution of ensemble probability distribution function (PDF) over time, plotted every 25 years, with probability on y-axis and Thwaites Glacier ice volume (in cm sea level equivalent; SLE) on x-axis. (b) Black lines are simulated ice volume contained in Thwaites Glacier catchment in cm SLE for all ensemble members. (c) Black dots are evolving grounding line migration rates for all ensemble members (based on the centroid of the 2D grounding line). (d) Snapshots (red, orange and pink lines) of grounding line positions at year 635 in model time, from 5th percentile, 50th percentile and 95th percentile ice volume ensemble members.

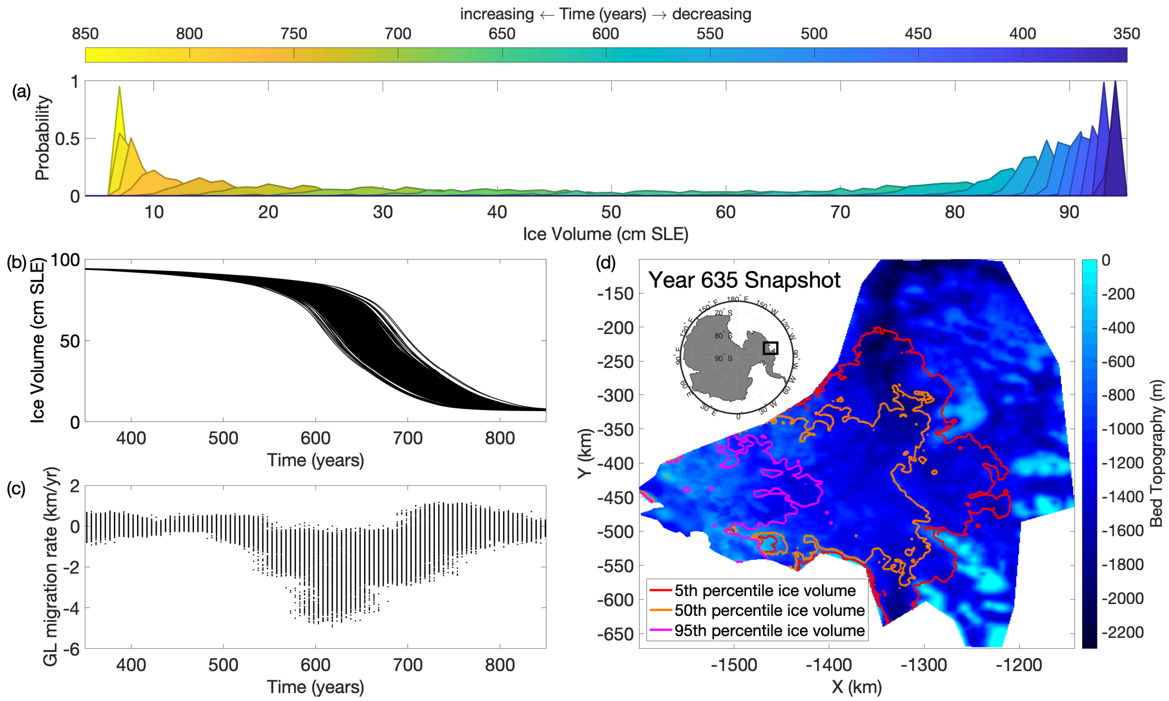

Fig. S4. Evolution of a 500-member ensemble of Ice Sheet System Model (ISSM) simulations of Thwaites glacier evolution over 500 years (where year zero in model time is the modern glacier state) in response to multidecadal variability ($\tau_F = 30$ yr) and constant average in maximum sub-ice shelf melt rate. (a) Evolution of ensemble probability distribution function (PDF) over time, plotted every 25 years, with probability on y-axis and Thwaites Glacier ice volume (in cm sea level equivalent; SLE) on x-axis. (b) Black lines are simulated ice volume contained in Thwaites Glacier catchment in cm SLE for all ensemble members. (c) Black dots are evolving grounding line migration rates for all ensemble members (based on the centroid of the 2D grounding line). (d) Snapshots (red, orange and pink lines) of grounding line positions at year 635 in model time, from 5th percentile, 50th percentile and 95th percentile ice volume ensemble members.

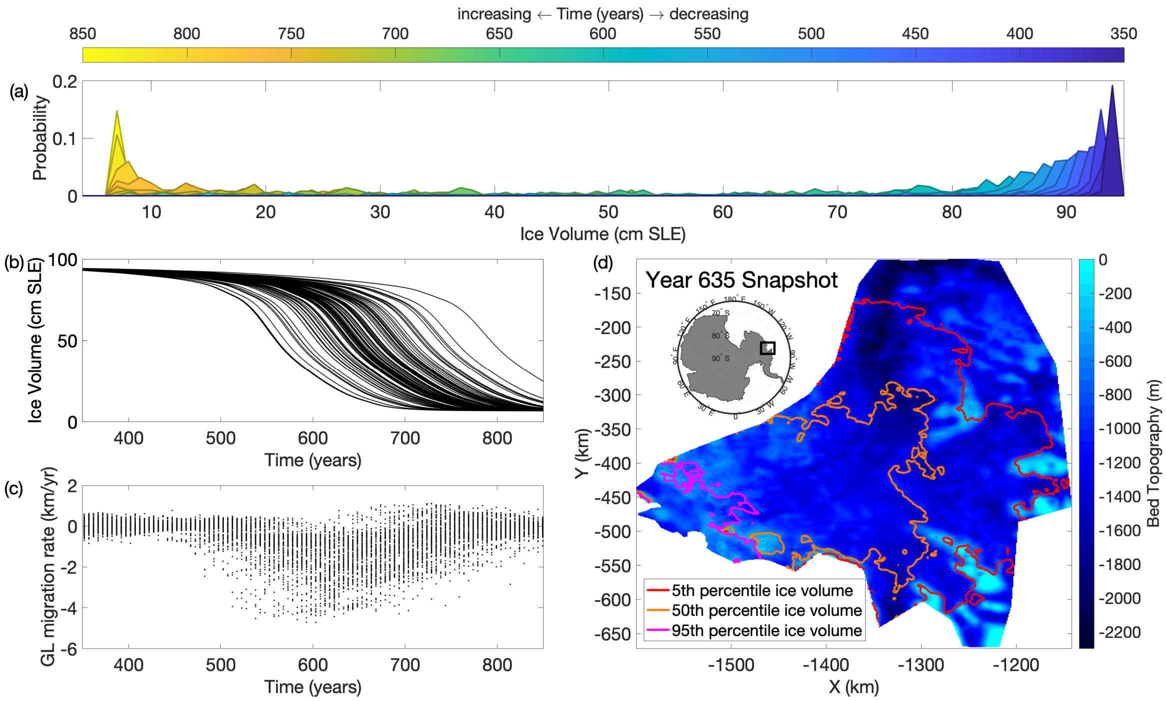

Fig. S5. Evolution of a 500-member ensemble of Ice Sheet System Model (ISSM) simulations of Thwaites glacier evolution over 500 years (where year zero in model time is the modern glacier state) in response to ocean forcing that is constant in time, but drawn from a Gaussian distribution for each individual ensemble member (mean 90 m/yr, standard deviation 5 m/yr). (a) Evolution of ensemble probability distribution function (PDF) over time, plotted every 25 years, with probability on y-axis and Thwaites Glacier ice volume (in cm sea level equivalent; SLE) on x-axis. (b) Black lines are simulated ice volume contained in Thwaites Glacier catchment in cm SLE for all ensemble members. (c) Black dots are evolving grounding line migration rates for all ensemble members (based on the centroid of the 2D grounding line). (d) Snapshots (red, orange and pink lines) of grounding line positions at year 635 in model time, from 5th percentile, 50th percentile and 95th percentile ice volume ensemble members.

Animations of ISSM Thwaites Glacier ensembles

Movie S1. Evolution of a 500-member ensemble of Ice Sheet System Model (ISSM) simulations of Thwaites glacier evolution over 500 years (where year zero in model time is the modern glacier state) in response to interannual variability ($\tau_F = 1.1$ yr) and constant average in maximum sub-ice shelf melt rate. Top left panel shows maximum melt rate (M_{max}) for a sample of 20 ensemble members. Top right panels shows evolving grounding line position for a sample of 20 ensemble members. Bottom panel shows the evolving probability distribution calculated from all ensemble members.

Movie S2. Evolution of a 500-member ensemble of Ice Sheet System Model (ISSM) simulations of Thwaites glacier evolution over 500 years (where year zero in model time is the modern glacier state) in response to interdecadal variability ($\tau_F = 10$ yr) and constant average in maximum sub-ice shelf melt rate. Top left panel shows maximum melt rate (M_{max}) for a sample of 20 ensemble members. Top right panels shows evolving grounding line position for a sample of 20 ensemble members. Bottom panel shows the evolving probability distribution calculated from all ensemble members.

Movie S3. Evolution of a 500-member ensemble of Ice Sheet System Model (ISSM) simulations of Thwaites glacier evolution over 500 years (where year zero in model time is the modern glacier state) in response to multidecadal variability ($\tau_F = 30$ yr) and constant average in maximum sub-ice shelf melt rate. Top left panel shows maximum melt rate (M_{max}) for a sample of 20 ensemble members. Top right panels shows evolving grounding line position for a sample of 20 ensemble members. Bottom panel shows the evolving probability distribution calculated from all ensemble members.

Movie S4. Evolution of a 500-member ensemble of Ice Sheet System Model (ISSM) simulations of Thwaites glacier evolution over 500 years (where year zero in model time is the modern glacier state) in response to ocean forcing that is constant in time, but drawn from a Gaussian distribution for each individual ensemble member (mean 90 m/yr, standard deviation 5 m/yr). Top left panel shows maximum melt rate (M_{max}) for a sample of 20 ensemble members. Top right panels shows evolving grounding line position for a sample of 20

ensemble members. Bottom panel shows the evolving probability distribution calculated from all ensemble members.

References

1. Moon W, Wettlaufer J (2013) A stochastic perturbation theory for non-autonomous systems. *Journal of Mathematical Physics* 54(12):123303.
2. Fitzmaurice A (2015) A Stochastic Approach to Examining the Seasonal Predictability of Arctic Sea Ice, (Woods Hole Oceanographic Institution GFD Summer School Reports), Technical report.
3. Robel AA, Roe G, Haseloff M (2018) Response of marine–terminating glaciers to forcing: Time scales, sensitivities, instabilities and stochastic dynamics. *Journal of Geophysical Research: Earth Surface.*
4. Tsai VC, Stewart AL, Thompson AF (2015) Marine ice-sheet profiles and stability under coulomb basal conditions. *Journal of Glaciology* 61(226):205–215.
5. Schoof C (2007) Marine ice-sheet dynamics. Part 1. The case of rapid sliding. *J. Fluid Mech.* 573:27–55.
6. Haseloff M, Sergienko OV (2018) The effect of buttressing on grounding line dynamics. *Journal of Glaciology* 64(245):417–431.
7. Roe GH, Baker MB (2016) The response of glaciers to climatic persistence. *Journal of Glaciology* 62(233):440–450.
8. Marshall J, Adcroft A, Hill C, Perelman L, Heisey C (1997) A finite-volume, incompressible navier stokes model for studies of the ocean on parallel computers. *Journal of Geophysical Research: Oceans (1978–2012)* 102(C3):5753–5766.
9. Losch M, Menemenlis D, Campin JM, Heimbach P, Hill C (2010) On the formulation of sea-ice models. part 1: Effects of different solver implementations and parameterizations. *Ocean Modelling* 33(1-2):129–144.
10. Jenkins A, Hellmer HH, Holland DM (2001) The role of meltwater advection in the formulation of conservative boundary conditions at an ice–ocean interface. *Journal of physical oceanography* 31(1):285–296.
11. Losch M (2008) Modeling ice shelf cavities in az coordinate ocean general circulation model. *Journal of Geophysical Research: Oceans* 113(C8).
12. Menemenlis D, et al. (2008) ECCO2: High resolution global ocean and sea ice data synthesis. *Mercator Ocean Quarterly Newsletter* 31:13–21.
13. Fenty I, Menemenlis D, Zhang H (2017) Global coupled sea ice-ocean state estimation. *Climate Dynamics* 49(3):931–956.
14. Seroussi H, et al. (2017) Continued retreat of Thwaites Glacier, West Antarctica, controlled by bed topography and ocean circulation. *Geophysical Research Letters.*
15. Menemenlis D, Fukumori I, Lee T (2005) Using Green's functions to calibrate an ocean general circulation model. *Monthly weather review* 133(5):1224–1240.
16. Onogi K, et al. (2007) The JRA-25 reanalysis. *Journal of the Meteorological Society of Japan. Ser. II* 85(3):369–432.
17. Holland DM, Jenkins A (1999) Modeling thermodynamic ice-ocean interactions at the base of an ice shelf. *Journal of Physical Oceanography* 29(8):1787–1800.
18. Dinniman MS, Klinck JM, Smith WO (2007) Influence of sea ice cover and icebergs on circulation and water mass formation in a numerical circulation model of the Ross Sea, Antarctica. *Journal of Geophysical Research: Oceans* 112(C11).
19. Schodlok MP, Menemenlis D, Rignot E, Studinger M (2012) Sensitivity of the ice-shelf/ocean system to the sub-ice-shelf cavity shape measured by NASA IceBridge in Pine Island Glacier, West Antarctica. *Annals of Glaciology* 53(60):156–162.
20. Schodlok M, Menemenlis D, Rignot E (2016) Ice shelf basal melt rates around Antarctica from simulations and observations. *Journal of Geophysical Research: Oceans* 121(2):1085–1109.
21. Gwyther DE, O'Kane TJ, Galton-Fenzi BK, Monselesan DP, Greenbaum JS (2018) Intrinsic processes drive variability in basal melting of the Totten Glacier Ice Shelf. *Nature Communications* 9(1):3141.
22. Larour E, Seroussi H, Morlighem M, Rignot E (2012) Continental scale, high order, high spatial resolution, ice sheet modeling using the Ice Sheet System Model (ISSM). *Journal of Geophysical Research: Earth Surface* 117(F1).
23. Morlighem M, et al. (2010) Spatial patterns of basal drag inferred using control methods from a full-stokes and simpler models for Pine Island Glacier, West Antarctica. *Geophysical Research Letters* 37(14).
24. Rignot E, Mouginot J, Scheuchl B (2011) Ice flow of the Antarctic ice sheet. *Science* 333(6048):1427–1430.
25. Seroussi H, Morlighem M, Larour E, Rignot E, Khazendar A (2014) Hydrostatic grounding line parameterization in ice sheet models. *The Cryosphere* 8(6):2075–2087.
26. Seroussi H, Morlighem M (2018) Representation of basal melting at the grounding line in ice flow models. *The Cryosphere* 12:3085–3096.
27. Fretwell P, et al. (2013) Bedmap2: improved ice bed, surface and thickness datasets for Antarctica. *The Cryosphere.*
28. Morlighem M, et al. (2011) A mass conservation approach for mapping glacier ice thickness. *Geophysical Research Letters* 38(19).
29. Lenaerts J, Van den Broeke M, van de Berg WJ, van Meijgaard E, Kuipers Munneke P (2012) A new, high-resolution surface mass balance map of antarctica (1979–2010) based on regional atmospheric climate modeling. *Geophysical Research Letters* 39(4).
30. Shapiro NM, Ritzwoller MH (2004) Inferring surface heat flux distributions guided by a global seismic model: particular application to Antarctica. *Earth and Planetary Science Letters* 223(1-2):213–224.